

# Independent Component-Based Spatiotemporal Clutter Filtering for Slow Flow Ultrasound

Jaime Tierney, Jennifer Baker, Daniel Brown, Don Wilkes, and Brett Byram, *Member, IEEE*

**Abstract**—Effective tissue clutter filtering is critical for non-contrast ultrasound imaging of slow blood flow in small vessels. Independent component analysis (ICA) has been considered by other groups for ultrasound clutter filtering in the past and was shown to be superior to principal component analysis (PCA)-based methods. However, it has not been considered specifically for slow flow applications or revisited since the onset of other slow flow-focused advancements in beamforming and tissue filtering, namely angled plane wave beamforming and full spatiotemporal singular value decomposition (SVD) (i.e., PCA-based) tissue filtering. In this work, we aim to develop a full spatiotemporal ICA-based tissue filtering technique facilitated by plane wave applications and compare it to SVD filtering. We compare ICA and SVD filtering in terms of optimal image quality in simulations and phantoms as well as in terms of optimal correlation to ground truth blood signal in simulations. Additionally, we propose an adaptive blood independent component sorting and selection method. We show that optimal and adaptive ICA can consistently separate blood from tissue better than principal component analysis (PCA)-based methods using simulations and phantoms. Additionally we demonstrate initial *in vivo* feasibility in ultrasound data of a liver tumor.

**Index Terms**—slow blood flow, power Doppler, clutter filter, ultrasound, independent component analysis

## I. INTRODUCTION

ULTRASOUND imaging of slow blood flow without contrast agents is difficult but desirable for several clinical applications, including detection of tumor blood flow for diagnosis and treatment monitoring and evaluation. One of the main challenges is tissue clutter interference with blood. Blood signal without contrast enhancement is weak compared to tissue and is closer to the noise floor. Therefore, clutter filtering is essential to extract weak blood signal. Conventional clutter filtering relies on clear spectral separation of tissue and blood in the slow-time frequency domain. This assumption is usually valid for blood flow in larger vessels with reasonable signal-to-noise ratios (SNR) and velocities that are faster than tissue motion caused by patient and sonographer hand motion. However, blood velocity in small vessels is slow and comparable to tissue velocity, resulting in a spectral overlap

in the slow-time frequency domain [1], [2]. Furthermore, the smallest, usually unresolvable, vessels are often randomly oriented, making it difficult to know the beam-to-flow angle for estimating velocity. For this reason, power Doppler imaging is used in this work and is generally best suited for slow flow imaging because it is relatively angle independent and computes the energy of the Doppler signal rather than velocity [3]. However, despite the advantages of power Doppler, slow flow imaging remains challenging due to tissue and noise interference with blood signal.

Tissue clutter filtering for ultrasound blood flow imaging has been thoroughly investigated for focused Doppler techniques [4]–[9]. Among the most common are infinite and finite impulse response filters (IIR and FIR, respectively) and polynomial regression filters [9]. Although effective for most blood flow imaging applications, the most common filtering techniques fail to preserve slow flow signal due to the spectral overlap problem in the slow-time frequency domain [1], [9]. Several eigen-based filtering techniques have been proposed as solutions to this problem because they operate in a domain other than the frequency domain and incorporate statistical information about the clutter and blood signals [10]–[13]. However, these methods require sufficient temporal sampling which is usually not achievable with conventional focused beamforming, which typically only has 8-16 slow-time samples [13]. To address this issue, angled plane wave beamforming was introduced in combination with principal component analysis (PCA)-based filtering [14]. Moreover, with sufficient temporal sampling and therefore reasonably similar spatiotemporal statistics, two-dimensional and higher order decompositions may be performed [14]–[16]. However, although these PCA-based techniques circumvent the frequency domain, they are not immune to overlap between tissue, blood, and noise components [16], [17], and they were shown to benefit from a time-domain adaptive tissue clutter demodulation technique that we developed previously to correct for tissue motion prior to filtering [18], [19]. This suggests that tissue motion can still cause an overlap between tissue and blood in the eigen-domain.

Independent component analysis (ICA)-based tissue filtering has also been considered and was previously shown to better separate blood from tissue and noise compared to PCA-based filters [12], [20]. As with PCA, ICA creates data driven basis functions that are intended to represent underlying source signals. ICA incorporates an added restriction that the basis functions be statistically independent, which will provide better separation for non-gaussian source signals. Although theoretically promising, ICA-based filtering has not been as

Copyright (c) 2019 IEEE. Personal use of this material is permitted. However, permission to use this material for any other purposes must be obtained from the IEEE by sending a request to pubs-permissions@ieee.org.

J. Tierney and B. Byram are with the Department of Biomedical Engineering, Vanderbilt University, Nashville, TN, USA (e-mail: jaime.e.tierney@vanderbilt.edu, brett.c.byram@vanderbilt.edu)

J. Baker and D. Brown are with the Department of Radiology, Vanderbilt University Medical Center, Nashville, TN, USA (e-mail: jennifer.c.baker@vanderbilt.edu, daniel.b.brown@vanderbilt.edu)

D. Wilkes is with the Department of Electrical Engineering and Computer Science, Vanderbilt University, Nashville, TN, USA (e-mail: mitch.wilkes@vanderbilt.edu)

extensively investigated as PCA-based filtering for ultrasound blood flow imaging, and its fundamental limits have yet to be evaluated with other slow flow-focused advancements, namely angled plane wave beamforming. Additionally, because it was applied to focused Doppler sequences in the time-domain, its potential as a full spatiotemporal filter has yet to be evaluated.

In this work, we aim to develop a spatiotemporal ICA-based filtering technique and compare it to SVD in terms of highest achievable image quality. Compared to our previous preliminary work [21], we aim to more thoroughly describe our ICA implementation and provide more substantial evidence for the benefit of ICA using single vessel phantoms and controlled simulations with ground truth blood signal. Additionally, we propose a novel adaptive blood independent component sorting and selection technique using a correlation-based sorting method and a K-means clustering approach to adaptively separate tissue and blood components. Furthermore, we apply these methods to multiple simulation and phantom realizations at different flow speeds, which extensively expands upon previous work for which we used amplitude thresholding for component sorting and selection and a single phantom realization for validation [22]. Furthermore, we demonstrate initial *in vivo* feasibility using liver tumor data.

## II. THEORY AND IMPLEMENTATION

### A. ICA Model

To outline our approach to ICA, we first assume a simple signal model as follows,

$$\mathbf{D} = \mathbf{C} + \mathbf{B} + \mathbf{N} \in \mathbb{R}^{Z \times L \times T} \quad (1)$$

where  $\mathbf{D}$  is our beamformed RF signal composed of tissue clutter ( $\mathbf{C}$ ), blood ( $\mathbf{B}$ ), and noise ( $\mathbf{N}$ ).  $\mathbb{R}^{Z \times L \times T}$  represents the set of real numbers with dimensions  $Z$ ,  $L$ , and  $T$  which are the total number of axial, lateral, and temporal samples, respectively. We use only real data for the analyses in this work to simplify the ICA implementation. As in PCA/SVD approaches to ultrasound clutter filtering [14], [15], we can reshape  $\mathbf{D}$  into a two-dimensional Casorati matrix,  $\mathbf{S} \in \mathbb{R}^{M \times T}$ , in space and time, where  $M = ZL$ . PCA techniques work by decomposing  $\mathbf{S}$  directly into its corresponding singular vectors and values. ICA generally works by solving for two unknowns,  $\mathbf{A} \in \mathbb{R}^{M \times Q}$  and  $\mathbf{X} \in \mathbb{R}^{Q \times T}$ , related to  $\mathbf{S}$  as follows,

$$\mathbf{S} = \mathbf{A}\mathbf{X} \quad (2)$$

where  $\mathbf{X}$  contains the unmixed source signals,  $\mathbf{A}$  is a mixing matrix containing the information for mixing the source signals in  $\mathbf{X}$  to produce  $\mathbf{S}$ , and  $Q$  represents the number of independent components. ICA involves two main steps: solving for  $\mathbf{A}$  and then using  $\mathbf{A}^{-1}$  to solve for  $\mathbf{X}$ . Many techniques exist for solving for  $\mathbf{A}$ . For our approach, we use a maximum likelihood (i.e., information maximization) method with BFGS optimization [23]–[25].

In our application of ICA, we use a transposed version of  $\mathbf{S}$ , with dimensions  $T$  by  $M$ . We also perform an initial dimensionality reduction on  $\mathbf{S}'$  to remove noise using SVD and the assumption that noise constitutes the lowest energy singular values [12]–[16]. We then perform the optimization

on the spatial singular vectors of  $\mathbf{S}'$  only, denoted  $\mathbf{Y}$ , as described below,

$$\mathbf{S}' = \mathbf{V}\boldsymbol{\lambda}\mathbf{U}' \in \mathbb{R}^{T \times M} \quad (3)$$

$$\mathbf{Y} = \boldsymbol{\lambda}\mathbf{U}' = \mathbf{A}\mathbf{X} \in \mathbb{R}^{E \times M} \quad (4)$$

where  $\mathbf{V} \in \mathbb{R}^{T \times E}$ ,  $\boldsymbol{\lambda} \in \mathbb{R}^{E \times E}$ , and  $\mathbf{U} \in \mathbb{R}^{E \times M}$  are the temporal singular vectors, singular values, and spatial singular vectors of  $\mathbf{S}'$ , respectively, with noise removed,  $\mathbf{A} \in \mathbb{R}^{E \times Q}$  is a square mixing matrix,  $\mathbf{X} \in \mathbb{R}^{Q \times M}$  contains the source signals, and  $E = Q$  is the number of principal and independent components corresponding to blood and tissue. We perform ICA on the de-noised, spatial singular vectors to minimize computational burden of the optimization algorithm. After solving for  $\mathbf{A}$ , we can multiply  $\mathbf{A}^{-1}$  by  $\mathbf{Y}$  to get  $\mathbf{X}$ .

Once the independent components are sorted and the principal and independent blood components are identified, as described in more detail in the following subsections, we can then reconstruct the blood signal as follows,

$$\mathbf{S}'_{blood} = \mathbf{V}^{T \times B_{PC}} \mathbf{A}^{B_{PC} \times B_{IC}} \mathbf{X}^{B_{IC} \times M} \in \mathbb{R}^{T \times M} \quad (5)$$

where  $B_{PC}$  and  $B_{IC}$  are the number of blood principal and independent components, respectively. Finally, we can transpose and reshape  $\mathbf{S}'_{blood}$  back to its original dimensions,  $\mathbf{B} \in \mathbb{R}^{Z \times L \times T}$ .

### B. ICA Rationale

The intention of unsupervised learning methods like PCA and ICA is to create more efficient representations of the underlying source signals compared to fixed bases such as the Fourier. In the case of tissue clutter filtering, the goal is to create bases that map tissue, blood and noise to distinct basis components that can be readily identified to isolate the blood. In practice, the basis components from PCA or ICA will typically have at least some overlap with all three types of physical source signals—blood, tissue and noise [16], [17]. The goal of PCA is to create uncorrelated bases that efficiently describe the data variance. The goal of ICA is to create statistically independent source bases, which also necessarily implies the bases are uncorrelated. When the underlying sources within the data are normally distributed multivariate random variables, uncorrelated signals are also independent, which means that ICA and PCA produce equivalent outcomes [26], [27].

In our implementation, ICA is not applied directly to the Casorati matrix so it is not attempting to directly separate tissue, blood and noise. ICA is applied to the spatial principal components so benefits realized from ICA only imply non-normality in the spatial dimension. After the initial dimensionality reduction to suppress noise and ease computation, we have a number of spatial principal components  $\mathbf{Y}_q$ . Despite the goals and assumptions of PCA, for any given principal vector,  $\mathbf{Y}_q$ , it is probable that both  $\sum \mathbf{B}\mathbf{Y}_q \neq 0$  and  $\sum \mathbf{C}\mathbf{Y}_q \neq 0$ . (Ideally there is no noise left, but in practice noise may still persist on many of the remaining principal vectors as well [17].) In other words, each of the spatial principal components will have some overlap of the underlying tissue and blood source signals. We attempt to improve this separation using

ICA on  $\mathbf{Y}$ . The assumption made is that at least some part of the blood or tissue has a non-normal distribution spatially that will allow for better separation using ICA. This seems at least plausible given the anatomically discrete nature of vessels. Additionally, for ICA to improve separation, it is not necessary that the sum of the underlying tissue source signals be uncorrelated to the sum of the underlying blood source signals (i.e.,  $\sum \mathbf{C}\mathbf{B} = 0$ ) or that  $\mathbf{C}$  or  $\mathbf{B}$  are themselves non-normal, but rather that there is some set of constructible independent components that individually have less simultaneous correlation with both  $\mathbf{C}$  and  $\mathbf{B}$ . To summarize, there is a plausible physical rationale for why ICA applied spatially may improve blood filtering. However, the bases formed by ICA, like PCA, have no fundamental connection to the underlying physics. Such bases are only a mathematical construct and attaching physical intuition is primarily a useful exercise for conceptualizing and developing filtering strategies. Therefore, a direct connection between ICA or PCA and the physics is not required as long as there exists an appropriate method for classifying each independent component as signal or noise (i.e. clutter).

### C. Independent Component Sorting

Unlike for principal components, which are, by definition, intuitively sorted by descending energy (i.e., tissue should be greater than blood which should be greater than noise), independent component ordering is challenging [26], [28]–[30]. For our implementation, we sort according to correlation coefficients computed between reconstructed power Doppler images made with each individual independent component  $q$  ( $PD_q$ ) and a power Doppler image made with all components ( $PD_Q$ ) as follows,

$$\rho_{sort}(q) = \frac{\sum (PD_Q \cdot * PD_q)}{\sqrt{\sum PD_Q^2} \sqrt{\sum PD_q^2}} \quad (6)$$

where  $PD_Q$  and  $PD_q$  are made by reshaping  $\mathbf{V}^{T \times E} \mathbf{A}^{E \times Q} \mathbf{X}^{Q \times M}$  and  $\mathbf{V}^{T \times E} \mathbf{A}_q^{E \times 1} \mathbf{X}_q^{1 \times M}$  using independent component  $q$  only, respectively, back to the original dimensions ( $Z$  by  $L$  by  $T$ ) and summing the squared values through slow-time. A power Doppler image made with all components is equivalent to a power Doppler image made with no tissue filtering for which tissue power will dominate since tissue signal is stronger than blood. Therefore, a component that produces a high correlation coefficient likely contains tissue while a component that produces a low correlation coefficient contains blood. Components that contain noise that persists after the initial dimensionality reduction will likely produce correlation coefficients that are more comparable to tissue due to noise being more uniformly distributed compared to blood. An example power Doppler image made with all components and corresponding correlation values are shown in Fig. 1a. Fig. 1c shows the corresponding power Doppler images made with each individual independent component (i.e.,  $PD_q$ ). The power Doppler images displayed in Fig. 1 have been log compressed and scaled for image quality purposes, but no log compression or scaling was done for the correlation sorting.

### D. Blood Component Selection

Once the independent components are sorted in  $\mathbf{A}\mathbf{X}$ , choosing the appropriate cutoff between tissue and blood is also challenging—a problem relevant for principal components as well. To determine whether or not ICA provides any additional benefit to PCA, it is worth comparing the two methods under optimal conditions. However, because it is impossible to determine optimal conditions clinically, adaptively identifying blood components is crucial.

To determine optimal cutoffs, we perform an exhaustive cutoff analysis using simulations and phantoms for which we know ground truth information. For SVD, we choose whichever cutoff  $k$  produces the highest image quality (IQ) correlation coefficient when compared to the blood only power Doppler image (for simulations) or whichever cutoff produces the best blood-to-background SNR image quality metric (for phantoms), as defined in the next section. The correlation coefficient computed for measuring simulation image quality is similar to Equation 6 as follows,

$$\rho_{IQ}(k) = \frac{\sum (PD_B \cdot * PD_k)}{\sqrt{\sum PD_B^2} \sqrt{\sum PD_k^2}} \quad (7)$$

where  $PD_B$  and  $PD_k$  are the power Doppler images made using blood only signal and made using principal or independent component  $k$  as the starting blood component, respectively. For these power Doppler images, a 2-dimensional spatial median filter, described in more detail in the next section, is applied before computing  $\rho_{IQ}$ . Additionally, a Fisher transformation was applied to all  $\rho_{IQ}$  values before taking the mean across realizations. An inverse Fisher transformation was then applied to the mean values for quantitative display. An example of a simulated blood only power Doppler image is shown in Fig. 1a. Figs. 1b and 1c show the corresponding power Doppler images made with each individual principal and independent component (i.e.,  $PD_k$ ). Again, the power Doppler images displayed in Fig. 1 have been log compressed and scaled for image quality purposes, but no log compression or scaling was done for the correlation computation. For ICA, we use the chosen optimal SVD cutoff for the temporal singular vector principal component filtering and then use whichever independent component cutoff produces the highest  $\rho_{IQ}$  or best SNR as described above. For both methods, we use a fixed noise cutoff to restrict variables, as indicated in the next section.

To determine adaptive cutoffs, we perform an initial adaptive singular value thresholding on the principal components. We threshold based on when the slope of the energy of the singular values goes below a certain value, as depicted in Fig. 1a [13], [15] and use this as the principal component cutoff for SVD filtering and ICA temporal singular vector filtering. Then, for the independent components, we perform a 100-iteration K-means clustering on  $\rho_{sort}$  (i.e., Equation 6) to group the coefficients into 3 groups. The number of groups chosen is based on the typical shape of the correlation coefficient curve, as shown in Fig. 1a, which has a steeper slope that flattens out before dropping again. Whichever group constitutes the independent component with the lowest  $\rho_{sort}$  value is the group identified as blood because blood should be the least

correlated to the no filter power Doppler image compared to tissue and noise. Although noise is mostly removed at this point, some will inevitably persist. Example optimal and adaptive cutoffs are depicted in Fig. 1a.

Our implementation of ICA results in both principal and independent component dimensions in the final reconstructed blood signal, as described in Equation 5. Therefore, both the principal and independent tissue components are removed when reconstructing the blood signal after applying ICA, resulting in two blood component selection techniques used for the ICA method, as described in the preceding two paragraphs.

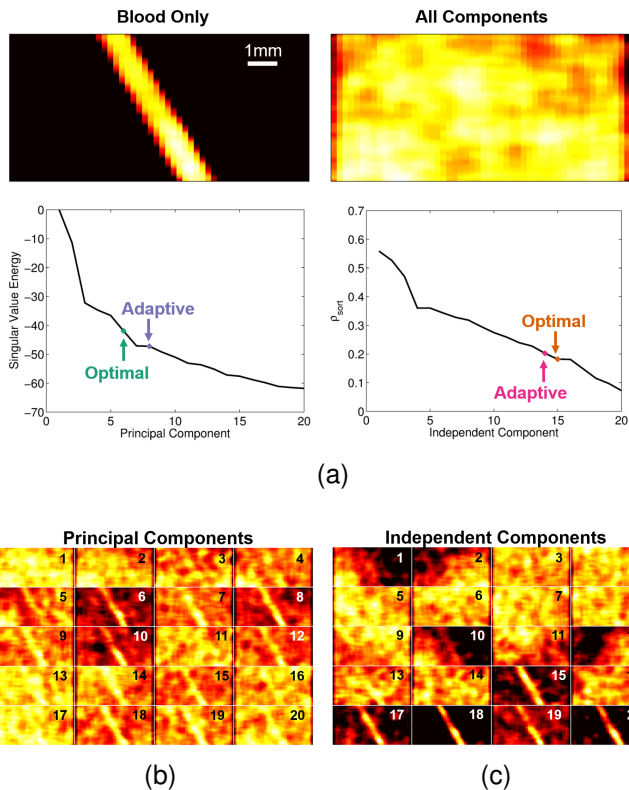


Fig. 1. Example simulation realization for a 400 sample slow-time ensemble. All displayed power Doppler images are scaled to individual maximums and a 20dB dynamic range. (a) The power Doppler image on the left depicts a case with blood flow only (i.e., no tissue or noise). The power Doppler image on the right shows a case with tissue, blood, and noise with no clutter filtering. The bottom row shows the energy of the singular values for each principal component on the left and the correlation coefficients (as computed in Equation 6) for each independent component on the right. Example adaptive and optimal cutoffs are shown for each case (SVD on the left and ICA on the right). A fixed noise cutoff of 20 was used for this example. Corresponding power Doppler images made with each individual principal and independent component are shown in (b) and (c), respectively.

### III. METHODS

#### A. Simulation Data

Field II [31] was used to simulate angled plane wave channel data of a 0.6 by 1cm area of tissue scatterers containing a 0.5mm diameter vessel of blood scatterers centered at a 2cm depth. Blood flow was laminar and moved at a peak velocity of 1mm/s. Tissue and blood scatterers were displaced using displacements estimated from 6 different hand motion phantom data sets to generate 6 realistic tissue motion realizations. For

the hand motion data sets, 6 volunteers acquired 3s of plane wave channel data ( $0^\circ$  at a pulse repetition frequency of 1kHz) of a stationary phantom (CIRS Model 040GSE, Norfolk, VA) using a Verasonics L12-5 probe and 7.8MHz center frequency down to a depth of 3cm. The channel data were beamformed, up-sampled to a sampling frequency of 62.5MHz, and band-pass filtered. Relative displacements were computed on the first second of data using a 2D autocorrelation approach [32] with an axial kernel size of  $1.25\lambda$  and lag of 1ms. Total displacements were computed by taking the cumulative sum of the relative displacements through slow-time. For each hand motion realization, the displacements were interpolated according to the location of the tissue and blood scatterers. To generate a blood only signal for computing ground truth filter performance (i.e., Eq. 7), tissue, blood and noise channel data were simulated and beamformed separately and then combined before applying tissue filtering. Blood and noise channel data were scaled to be 40dB lower than tissue signal.

#### B. Phantom Data

Eight different phantoms were made using a polyvinyl alcohol and graphite mixture and 1 freeze-thaw cycle. Each phantom had a 0.6mm diameter wall-less vessel within a 2 by 3cm mold. Using a syringe pump, blood mimicking fluid (CIRS Model 046, Norfolk, VA) flowed through each phantom vessel at average velocities of either 1mm/s or 5mm/s. To ensure 6 different realizations for each flow speed, 6 different phantoms were used for each case. A hand held Verasonics L12-5 probe was used to acquire plane wave channel data for each realization for each flow speed.

#### C. In Vivo Data

Plane wave channel data were acquired from a patient with a 4.6cm-diameter hepatocellular carcinoma (HCC) lesion located in segment 2 of the liver right above the portal vein. HCC tumors are known to be highly vascularized and blood flow characteristics are used for treatment and diagnosis [33]. Informed written consent in accordance with Vanderbilt's Institutional Review Board was obtained from the patient prior to the start of the acquisition. Using a Verasonics C5-2 probe, an interventional radiologist acquired 333ms of angled plane wave channel data.

#### D. Image Acquisition and Beamforming

Channel data were acquired at a 7.8MHz transmit center frequency for the simulation and phantom experiments and a 4.2MHz transmit center frequency for the *in vivo* data. For all experiments, 9 angled plane waves evenly spaced between  $-8^\circ$  and  $8^\circ$  were transmitted at pulse repetition frequencies (PRF) of 9kHz for 1s (simulation and phantom) or 5.4kHz for 333ms (*in vivo*). Channel data were beamformed using parallel receive beamforming and consecutive angles were summed to synthesize transmit focusing, resulting in final PRFs of 1kHz (simulation and phantom) and 600Hz (*in vivo*) [34] and ensemble sizes of 1000-samples (simulation and phantom) and 200-samples (*in vivo*). Hann apodization and

aperture growth to achieve an F/# of 2 were implemented during receive beamforming. Beamformed data were band-pass filtered after being up-sampled by factors of 2 and 3 to achieve sampling frequencies of 62.5MHz (simulation and phantom) and 50MHz (*in vivo*). Additionally, for *in vivo* anatomical reference, immediately prior to the acquisition of the plane wave scan, a conventional focused scan was acquired at 6cm.

### E. Post-Processing

Ensemble sizes between 20 samples (20ms) and 1000 samples (1s) were used for tissue filtering and power Doppler estimation for each simulation and phantom data set. SVD and ICA tissue filtering were implemented as described in the previous section using 20, 30, and 40 as the principal component noise cutoff for the simulations, 1mm/s phantom data and 5mm/s phantom data, respectively (i.e.,  $E = 20$  or  $E = 30$  or  $E = 40$ ). For the phantom data, a noise cutoff of 20 was used for the 20 sample ensemble.

For the *in vivo* example, ensemble sizes of 120, 160, and 200 samples (200ms, 267ms, and 333ms) were evaluated. SVD, ICA and a conventional 50Hz 6th order Type 1 Chebyshev IIR high-pass filter were compared. A fixed noise cutoff of 40 (i.e.,  $E=40$ ) was used for SVD and ICA filtering.

Power Doppler was computed using  $PD(z, x) = \sum_{t=1}^T d(z, x, t)^2$ , where  $d(z, x, t)$  is beamformed and filtered RF signal at axial position  $z$ , lateral position  $x$ , and slow-time point  $t$ , for each data set. A 1mm by 1mm spatial median filter was applied to each power Doppler image for the simulations and phantoms. A 0.4mm by 0.4mm spatial median filter was applied to the *in vivo* power Doppler images. For simulated data, correlation coefficients (compared to blood only power Doppler, i.e.,  $\rho_{IQ}$ ) were computed as in Equation 7. For all data, blood-to-background SNR, contrast-to-noise ratio (CNR) and generalized contrast-to-noise ratio (GCNR) [35] were computed as follows,

$$SNR = 10\log_{10} \frac{\frac{1}{N} \sum_{i=1}^N PD_{sig}(i)}{\frac{1}{M} \sum_{i=1}^M PD_{bkgd}(i)} \quad (8)$$

$$CNR = 10\log_{10} \frac{|\frac{1}{N} \sum_{i=1}^N PD_{sig}(i) - \frac{1}{M} \sum_{i=1}^M PD_{bkgd}(i)|}{STD(\frac{1}{M} \sum_{i=1}^M PD_{bkgd}(i))} \quad (9)$$

$$GCNR = 1 - OVL \quad (10)$$

where  $N$  and  $M$  are the total number of pixels in the vessel and background, respectively,  $PD_{sig}$  and  $PD_{bkgd}$  are the power Doppler values in the vessel and background, respectively, STD stands for the standard deviation, and  $OVL$  represents the overlap between histograms of the background and vessel pixels. The entire region outside of the simulation or phantom vessel was considered as background. A background region was chosen for the *in vivo* data as indicated in Fig. 10. Power Doppler images were made by log compressing the power Doppler signal ( $I = 10\log_{10} PD(z, x)$ ). Images were scaled to individual maximums and dynamic ranges were chosen for the simulation and phantom data by computing the average power value of the background pixels for each image.

This value was used as the minimum value in the image. For the *in vivo* data, the images were scaled to a 15dB dynamic range.

### F. Optimal Blood Component Selection

For computing optimal image quality metrics, simulation and phantom data were filtered using tissue cutoffs between 1 and  $E$  for SVD and between 1 and  $Q$  for ICA for each realization and ensemble. When reconstructing power Doppler images with ICA, a fixed principal component cutoff was used for temporal singular vector filtering. As described in the previous section, for simulations, the principal component cutoff that produced the highest SVD  $\rho_{IQ}$  (Equation 7) was used as the cutoff for temporal singular vector filtering. For phantoms, the principal components that produced the highest SVD SNR was used for temporal singular vector filtering.

### G. Adaptive Blood Component Selection

As described in the previous section, the cutoff between tissue and blood principal components was chosen by computing when the slope of the singular values goes below a certain threshold. The same threshold was used for all ensemble sizes for each filter case. Thresholds of 2, 1, 0.5, and 1 were used for determining the principal component cutoff between tissue and blood for the simulations, 1mm/s phantoms, 5mm/s phantoms, and *in vivo* data, respectively.

To determine the independent component cutoff between tissue and blood, a K-means clustering was performed and is described in more detail in Section II-C.

## IV. RESULTS

### A. Simulations

The simulation results demonstrate that ICA can remove tissue clutter better than SVD by itself both optimally and adaptively for all ensemble sizes tested. Fig. 2 shows the optimal and adaptive results for an example realization using a 400-sample ensemble. For this example, the adaptive ICA K-means approach chose the cutoff that produced the highest achievable correlation to the blood only power Doppler image. The same was not true for SVD, but the singular value thresholding approach chose a cutoff that was reasonably close to the optimal cutoff. The ICA power Doppler images show better clutter suppression and more uniform flow through the vessel than both the optimal and adaptive SVD cases.

These qualitative results are supported quantitatively in Figs. 3 and 4. Fig. 3 shows the correlation coefficients ( $\rho_{IQ}$ ) computed for each ensemble size for optimal and adaptive ICA and SVD. Optimal ICA produces correlation coefficients that are consistently higher than optimal SVD. The same is true for adaptive ICA compared to adaptive SVD. Adaptive ICA also produces correlation coefficients that are higher than optimal SVD for larger ensemble sizes, as shown in the plot overlaying both optimal and adaptive results.

Fig. 4 shows the simulation image quality results for the optimal and adaptive ICA and SVD approaches. Similar to the correlation coefficients, optimal ICA produces higher SNR, CNR, and GCNR than optimal SVD. The same is true for adaptive ICA compared to adaptive SVD.

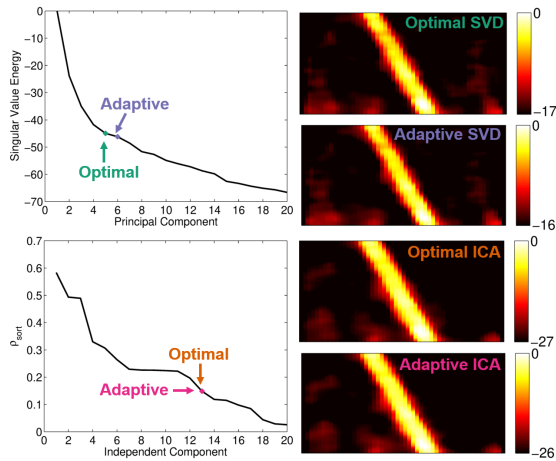


Fig. 2. Optimal and adaptive simulation results for a single realization using a 400-sample ensemble. Singular values are shown for each principal component in the top left. The optimal and adaptively selected principal component cutoffs are indicated in teal and purple. Correlation coefficients for each independent component (Equation 6) are shown in the bottom left plot. Optimal and adaptively selected independent component cutoffs are indicated in pink and orange, respectively, and are equivalent for this case. Corresponding optimal and adaptive SVD and ICA power Doppler images are shown on the right on dB scales. Each image is scaled to the mean of the background pixels resulting in different dynamic ranges.

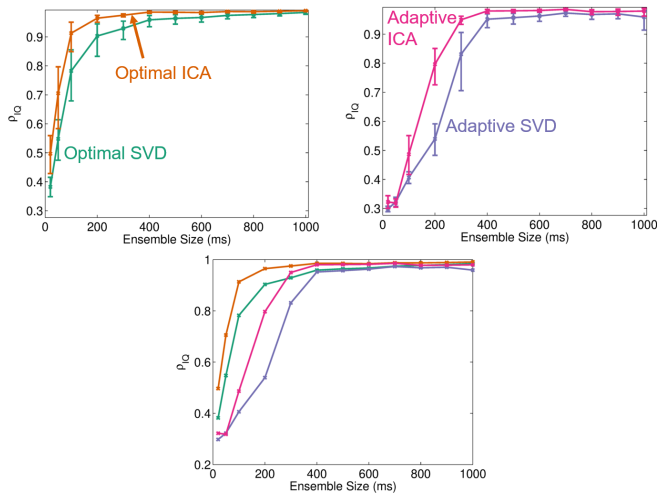


Fig. 3. Simulated average correlation coefficients computed using Equation 7 are shown for ensemble sizes between 20 and 1000-samples (i.e., 20ms and 1s). Optimal and adaptive results are shown in the top left and right, respectively. Error bars indicate standard error. The plot on the bottom has both optimal and adaptive results without error bars for visualization purposes.

### B. Phantoms

Similar to the simulation results, ICA is shown to produce superior image quality compared to SVD with the 1mm/s and 5mm/s phantom data both optimally and adaptively. Fig. 5 shows results for a single 1mm/s phantom data set using a 400-sample ensemble. For this example, the adaptive SVD approach chose the tissue cutoff that produces optimal SNR, therefore the adaptive and optimal SVD power Doppler images are the same. The adaptive ICA method did not result in the same tissue cutoff that produces optimal SNR, but it did result in a cutoff that produces an image that has arguably better

background suppression than the optimal case. The optimal ICA image has brighter blood pixels and more uniform flow across the vessel laterally than the adaptive ICA image, but the tissue clutter below the vessel is suppressed better with adaptive ICA. Additionally, both the adaptive and optimal ICA images demonstrate better tissue clutter suppression than the optimal and adaptive SVD image.

Similar qualitative conclusions can be made for the 5mm/s phantom example shown in Fig. 6 for a 400-sample ensemble. For this case, the adaptive SVD approach chose a tissue cutoff that does not produce exactly optimal SNR, but produced very close to optimal image quality. Similarly, adaptive ICA did not choose an optimal tissue cutoff, but it produced image quality that is very similar to the optimal ICA case. The ICA and SVD images for this case are similar, but ICA produces more uniform flow throughout the vessel. Although subtle, the improvement with ICA is not insignificant, especially for low SNR small vessel environments.

Optimal and adaptive ICA produced higher SNR, CNR, and GCNR for most ensemble sizes compared to optimal and adaptive SVD, respectively, as shown in Figs. 7 and 8 for both phantom data sets. For the 1mm/s phantom data, GCNR is higher when using SVD for the smallest ensemble sizes. This is likely because of no flow being detected in the vessel, which would result in a clear separation between bright tissue clutter in the background region and dark blood signal in the vessel. GCNR as we have implemented it does not account for negated trends.

Although the adaptive ICA approach does not produce the same image quality as optimal ICA, it does produce better image quality than optimal SVD for larger ensemble sizes. This was demonstrated in Fig. 3, and is also supported in Fig. 9 which overlays all SNR results for varying ensemble sizes for the simulations, 1mm/s phantom data, and 5mm/s phantom data. The improvement with adaptive ICA is most apparent with the simulation and 1mm/s phantom data.

### C. In Vivo

To demonstrate *in vivo* feasibility, adaptive SVD and ICA were applied to data of a HCC tumor in the liver. Fig. 10 shows example focused B-mode, angled plane wave B-mode, and power Doppler images made with no filtering, adaptive SVD, adaptive ICA, and conventional IIR filtering. Compared to the image with no tissue filtering, a small vessel is clearly seen in all of the cases with tissue filtering. However, the image made using ICA shows better clutter suppression compared to those using IIR or SVD filtering. Also, quantitatively, ICA produced the highest image quality metrics overall compared to IIR and SVD filtering.

### D. Computation Time

Fig. 11 demonstrates the added computational time needed to perform the proposed ICA technique for each ensemble size for the simulations, phantoms, and *in vivo* data. As expected, computation time increases with larger fixed noise cutoffs which results in ICA optimizing over more tissue and blood components. Also, computation time increases when larger

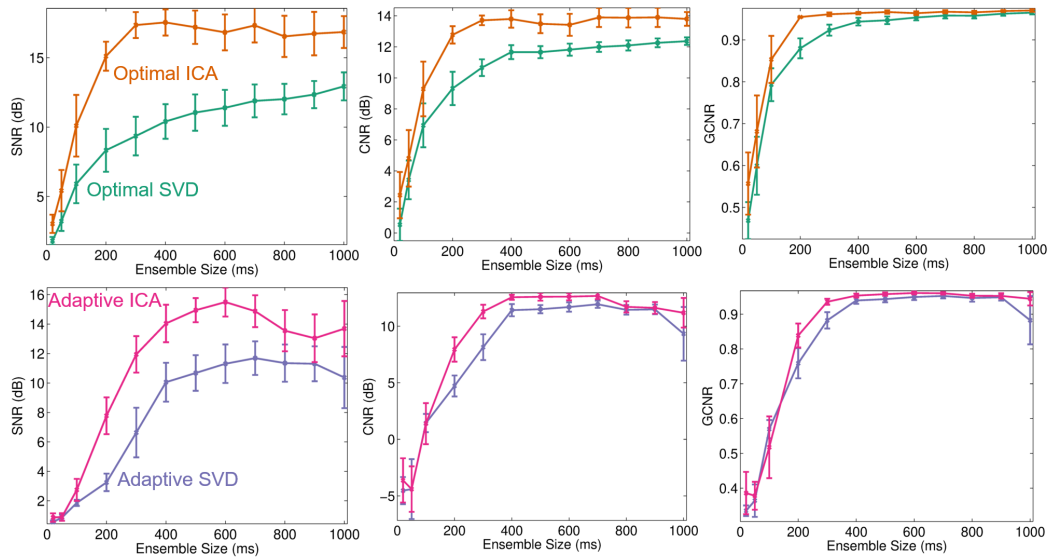


Fig. 4. Simulated average SNR (left), CNR (middle), and GCNR (right) are shown for ensemble sizes between 20 and 1000-samples (i.e., 20ms and 1s). Optimal ICA (orange) and optimal SVD (teal) are shown in the top row. Adaptive ICA (pink) and adaptive SVD (purple) are shown in the bottom row. Error bars indicate standard error.

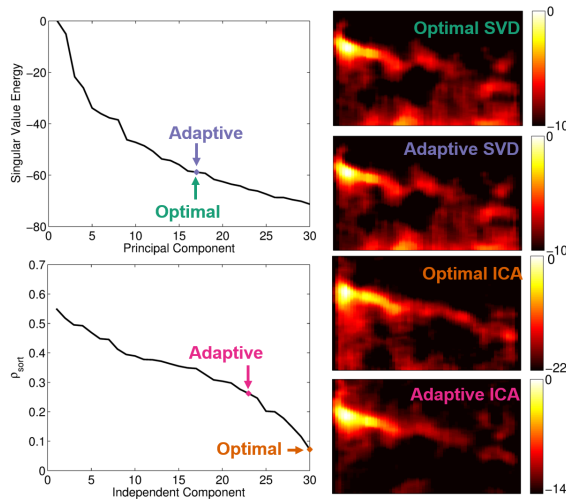


Fig. 5. Optimal and adaptive 1mm/s phantom results for a single realization using a 400-sample ensemble. Singular values are shown for each principal component in the top left. The optimal and adaptively selected principal component cutoffs are indicated in teal and purple, respectively, and are equivalent for this case. Correlation coefficients for each independent component (Equation 6) are shown in the bottom left plot. Optimal and adaptively selected independent component cutoffs are indicated in pink and orange, respectively. Corresponding optimal and adaptive SVD and ICA power Doppler images are shown on the right on dB scales. Each image is scaled to the mean of the background pixels resulting in different dynamic ranges.

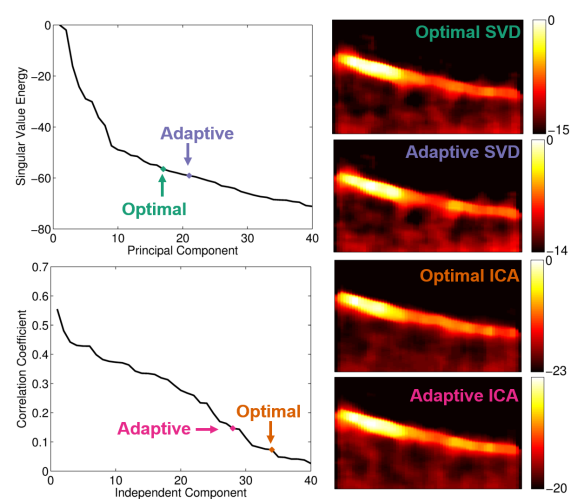


Fig. 6. Optimal and adaptive 5mm/s phantom results for a single realization using a 400-sample ensemble. Singular values are shown for each principal component in the top left. The optimal and adaptively selected principal component cutoffs are indicated in teal and purple, respectively. Correlation coefficients for each independent component (Equation 6) are shown in the bottom left plot. Optimal and adaptively selected independent component cutoffs are indicated in pink and orange, respectively. Corresponding optimal and adaptive SVD and ICA power Doppler images are shown on the right on dB scales. Each image is scaled to the mean of the background pixels resulting in different dynamic ranges.

spatial fields of view are used as was the case for the phantom data compared to the simulations.

## V. DISCUSSION

The exhaustive search for optimal tissue cutoffs demonstrates the achievable benefit of ICA-based filtering compared to SVD by itself. In all simulation and phantom experiments, ICA produced the highest optimal SNR, CNR, and GCNR

overall as well as the most qualitatively compelling images of tissue clutter suppression. Although it is meaningful that ICA produces the highest values across multiple image quality metrics, it is difficult to draw definitive conclusions based on these metrics due to their inherent biases and differences [19], [35]. We address this concern by making use of controlled simulations with which we were able to compare filtered images to ground truth blood signal. The correlation coeffi-

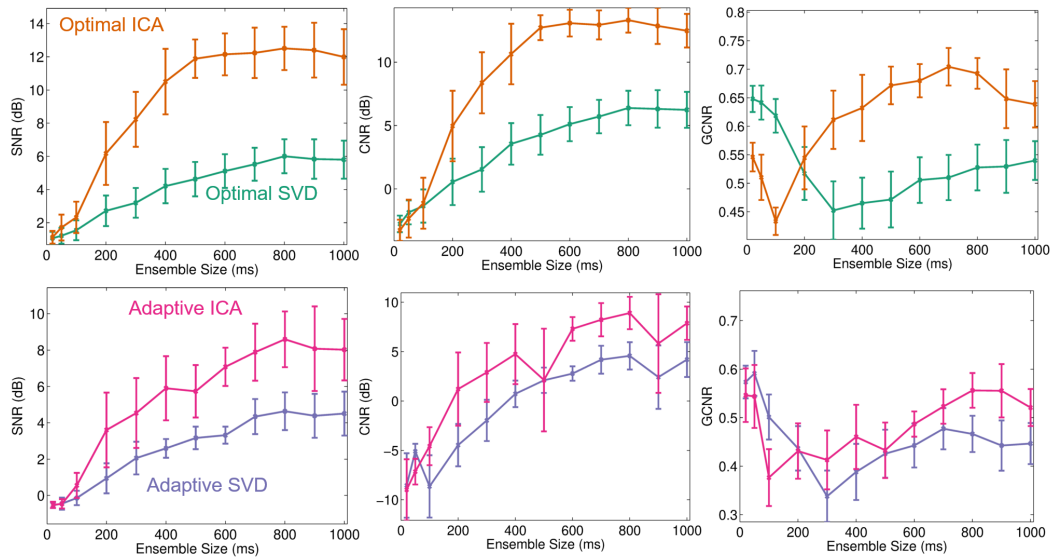


Fig. 7. Average SNR (left), CNR (middle), and GCNR (right) are shown for ensemble sizes between 20 and 1000-samples (i.e., 20ms and 1s) for the 1mm/phantom data. Optimal ICA (orange) and optimal SVD (teal) are shown in the top row. Adaptive ICA (pink) and adaptive SVD (purple) are shown in the bottom row. Error bars indicate standard error.

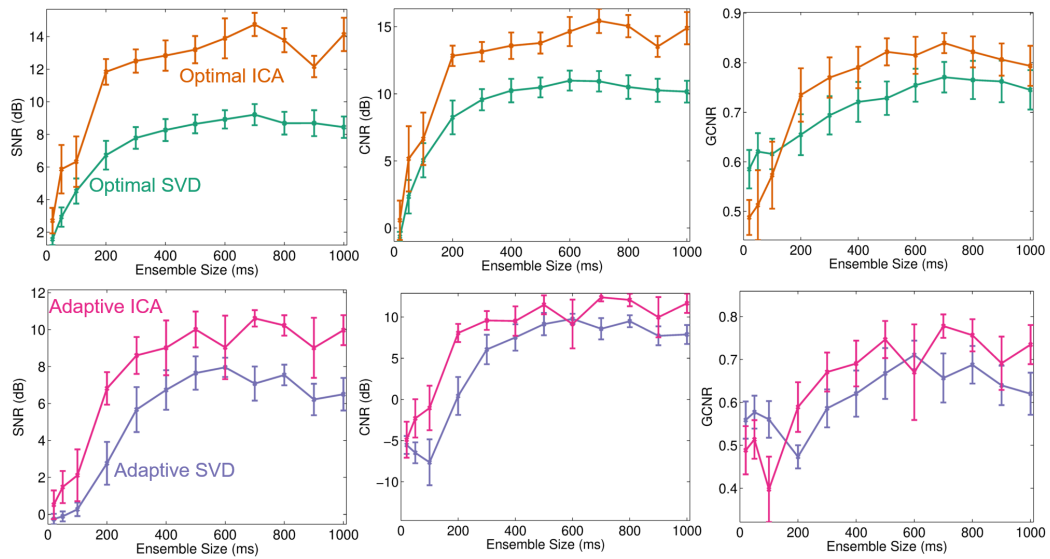


Fig. 8. Average SNR (left), CNR (middle), and GCNR (right) are shown for ensemble sizes between 20 and 1000-samples (i.e., 20ms and 1s) for the 5mm/phantom data. Optimal ICA (orange) and optimal SVD (teal) are shown in the top row. Adaptive ICA (pink) and adaptive SVD (purple) are shown in the bottom row. Error bars indicate standard error.

clients computed against this ground truth signal provide more substantial evidence for the potential benefit of ICA-based filtering compared to SVD by itself.

This work is the first to assess ICA-based filtering using ground truth simulations in combination with other slow flow ultrasound advancements, namely angled plane wave beamforming. Compared to conventional Doppler beamforming, plane wave sequences have enabled much longer ensembles to be achieved while maintaining reasonable frame-rates. The results in this work demonstrate the benefit of long ensembles for ICA filtering, as shown with ground truth correlation estimates as well as image quality metrics. Similar to conclusions

made in previous work for SVD filtering [19], the ICA metrics evaluated in this manuscript appear to plateau at larger ensembles, which could be indicative of a fundamental limit or an unaccounted for source of decorrelation. However, fixed noise cutoffs were used for both simulations and phantoms which could also explain the plateau, assuming the noise cutoff does not apply equally well to all ensemble sizes. Specifically, for small ensemble sizes, noise was likely not fully removed for all realizations with the fixed noise cutoffs used in this work. In contrast, for larger ensemble sizes, blood likely spanned to components above the fixed noise cutoff and was removed during the noise filtering. To account for this shortcoming,

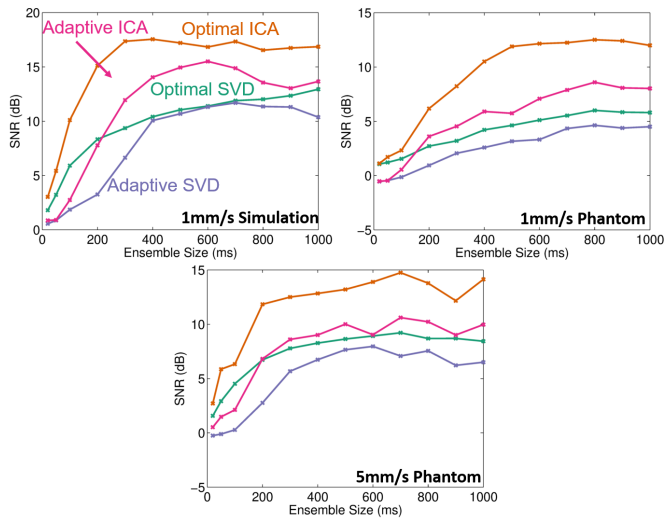


Fig. 9. Average SNR for varying ensemble sizes is shown for simulations (top left), 1mm/s phantom data (top right) and 5mm/s phantom data (bottom). SNR produced using optimal ICA (orange), adaptive ICA (pink), optimal SVD (teal), and adaptive SVD (purple) are shown on each plot.

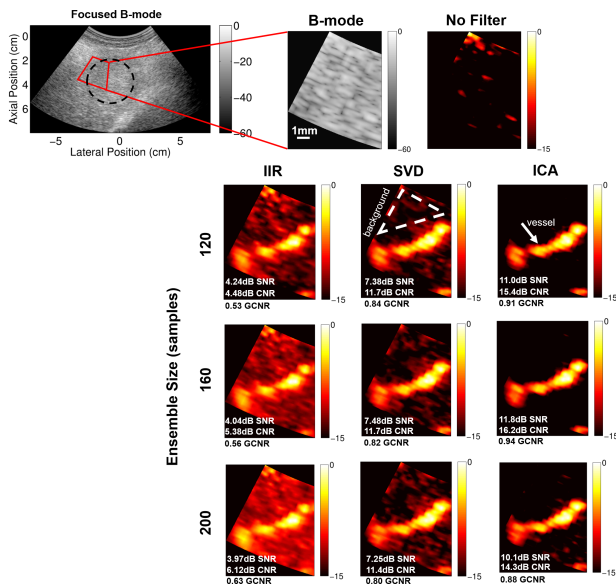


Fig. 10. *In vivo* data of a HCC tumor in the liver. A full field of view focused B-mode image is shown for reference in the top left. The tumor is outlined in black and the field of view used to make power Doppler images is outlined in red and indicated by the angled plane wave B-mode image in the top center. A no filter power Doppler image is shown next to the B-mode images. Below these, power Doppler images were made using 120, 160, and 200-sample ensemble sizes with a 50Hz IIR filter (left column), adaptive SVD filtering (middle column) and adaptive ICA filtering (right column). All images are scaled to a 15dB dynamic range. SNR, CNR, and GCNR values are displayed on each image. The background pixels used in these measurements are indicated in the 120 sample ensemble SVD image.

future work will aim to incorporate adaptive noise filtering in addition to the adaptive ICA and SVD techniques used in this work.

Although it was useful to compute highest achievable metrics to determine the true potential of each technique, it is not practical or possible *in vivo*. In this work we propose a

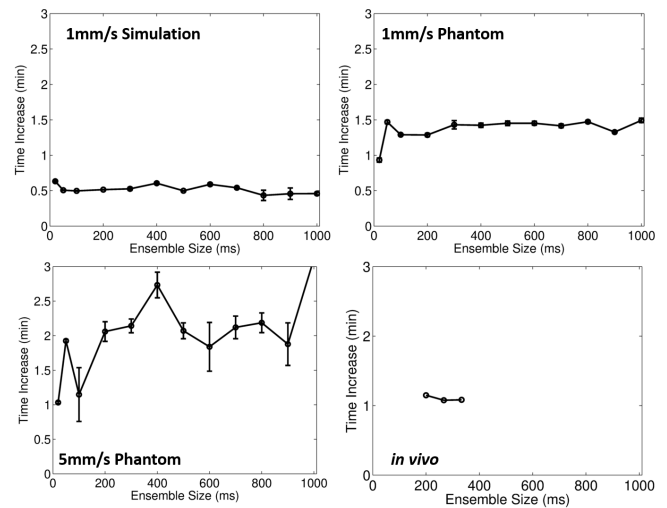


Fig. 11. Computation time increase in minutes for ICA compared to SVD for the simulations (top left), 1mm/s phantom (top right), 5mm/s phantom (bottom left), and *in vivo* (bottom right) data for each ensemble size evaluated. For the simulation and phantom data, the difference in computation times were averaged over realizations and error bars reflect the standard error of the mean.

novel adaptive K-means clustering approach in combination with simple singular value thresholding to adaptively select blood independent and principal components, respectively. The simulation and phantom results demonstrate that adaptive ICA can produce higher metrics than adaptive SVD and, for larger ensembles, optimal SVD. Additionally, the *in vivo* example supports these conclusions and shows improvements in small vessel visualization with adaptive ICA filtering compared to adaptive SVD. Although effective for the purposes of this work, the singular value thresholding technique is likely not optimal for determining blood principal components. Several more advanced adaptive SVD approaches that also incorporate noise filtering have been proposed [15], [36] that would likely improve the adaptive SVD metrics. However, our results suggest that adaptive ICA will similarly benefit from these more advanced principal component cutoff selection techniques. Additionally, for our initial implementation, we perform K-means clustering on correlation values only, but other features, such as the power of each independent component or the root mean square error compared to the no filtering image, could also be included to potentially improve accuracy and facilitate another level of sorting.

Finally, as mentioned previously, there are many ICA methods that exist. In this work we used an information maximization approach [23]–[25], and previously Gallippi and Trahey used the joint approximation diagonalization of eigen-matrices (JADE) algorithm [12], [20]. Other methods, including fourth-order blind identification (FOBI) and fast ICA, should also be evaluated to determine which is best suited for the spatiotemporal clutter filtering application. Additionally, input dimensionality should also be considered. For our implementation we perform ICA on the spatial singular vectors. It is worth investigating further how ICA performs on temporal singular vectors or if there is value in combining both spatial and temporal singular vector ICA filtering. Without

these analyses, it is possible that the true potential of ICA has yet to be realized.

There are a few additional shortcomings of the proposed methods that should be addressed with future work. First, the simulation and phantom experiments do not include vessel wall motion due to pulsatile flow or multiple randomly oriented vessels, and it would be worthwhile to evaluate these techniques on additional representative arterial and slow flow simulations and phantoms. Additionally, computation time was not the focus of this work, but ICA is generally more computationally expensive compared to SVD, as shown in Fig. 11, and real-time applications will likely be more difficult to realize. However, several factors, including the ICA optimization method, spatial field of view, and number of input principal components, will greatly impact computation time and should be considered in a larger parameter study focused on real-time implementation. In addition to improving computation time, smaller spatial fields of view were observed to improve the ICA optimization. Therefore, to realize a full field-of-view implementation of ICA, we think that block-wise approaches could be implemented as was done for SVD techniques [15].

## VI. CONCLUSION

ICA was previously considered for ultrasound tissue filtering, but it has not been revisited since the proposal of recent slow flow-focused advancements. Additionally, controlled simulations with ground truth blood signal have not been previously used for determining the fundamental potential of both SVD and ICA. Furthermore, adaptive independent component sorting and selection has not been previously proposed or investigated for the purposes of ultrasound slow blood flow imaging. We address these shortcomings by developing a spatiotemporal ICA-based filtering technique using angled plane wave beamforming and evaluate it in comparison to the well-known SVD filter. We show that optimal and adaptive ICA can produce image quality metrics that are superior to optimal and adaptive SVD across varying ensemble sizes using simulations and phantom data. Furthermore, we demonstrate initial *in vivo* feasibility in a liver tumor data set.

## ACKNOWLEDGMENT

The authors would like to thank the staff of the Vanderbilt University ACCRE computing resource. This work was supported in part by NIH grants 1R35HL135790-01 and S10OD016216-01 and NSF award IIS-1750994.

## REFERENCES

- [1] A. Heimdal and H. Torp, "Ultrasound doppler measurements of low velocity blood flow: limitations due to clutter signals from vibrating muscles," *IEEE Transactions on Ultrasonics, Ferroelectrics and Frequency Control*, vol. 44, pp. 873–881, 1997.
- [2] C. Tremblay-Darveau, R. Williams, L. Milot, M. Bruce, and P. N. Burns, "Combined perfusion and doppler imaging using plane-wave nonlinear detection and microbubble contrast agents," *IEEE Transactions on Ultrasonics, Ferroelectrics and Frequency Control*, vol. 61, pp. 1988–2000, 2014.
- [3] J. M. Rubin, R. S. Adler, J. B. Fowlkes, S. Spratt, J. E. Pallister, J.-F. Chen, and P. L. Carson, "Fractional moving blood volume: estimation with power doppler us," *Radiology*, vol. 197, no. 1, pp. 183–190, 1995.
- [4] A. Hoeks, J. Van de Vorst, A. Dabekausen, P. Brands, and R. Reneman, "An efficient algorithm to remove low frequency doppler signals in digital doppler systems," *Ultrasonic imaging*, vol. 13, no. 2, pp. 135–144, 1991.
- [5] L. Thomas and A. Hall, "An improved wall filter for flow imaging of low velocity flow," *IEEE Ultrasonics Symposium Proceedings*, vol. 3, pp. 1701–1704, 1994.
- [6] A. P. Kadi and T. Loupas, "On the performance of regression and step-initialized iir clutter filters for color doppler systems in diagnostic medical ultrasound," *IEEE transactions on ultrasonics, ferroelectrics, and frequency control*, vol. 42, no. 5, pp. 927–937, 1995.
- [7] H. Torp, "Clutter rejection filters in color flow imaging: A theoretical approach," *IEEE transactions on ultrasonics, ferroelectrics, and frequency control*, vol. 44, no. 2, pp. 417–424, 1997.
- [8] S. Bjaerum, H. Torp, and K. Kristoffersen, "Clutter filter design for ultrasound color flow imaging," *IEEE Transactions on Ultrasonics, Ferroelectrics, and Frequency Control*, vol. 49, pp. 204–216, 2002.
- [9] —, "Clutter filters adapted to tissue motion in ultrasound color flow imaging," *IEEE Transactions on Ultrasonics, Ferroelectrics, and Frequency Control*, vol. 49, pp. 693–704, 2002.
- [10] L. A. Ledoux, P. J. Brands, and A. P. Hoeks, "Reduction of the clutter component in doppler ultrasound signals based on singular value decomposition: a simulation study," *Ultrasonic imaging*, vol. 19, no. 1, pp. 1–18, 1997.
- [11] L. Lovstakken, S. Bjaerum, K. Kristoffersen, R. Haaverstad, and H. Torp, "Real-time adaptive clutter rejection filtering in color flow imaging using power method iterations," *IEEE transactions on ultrasonics, ferroelectrics, and frequency control*, vol. 53, no. 9, pp. 1597–1608, 2006.
- [12] C. Gallippi and G. Trahey, "Adaptive clutter filtering via blind source separation for two-dimensional ultrasonic blood velocity measurement," *Ultrasonic Imaging*, vol. 24, pp. 193–214, 2002.
- [13] A. C. H. Yu and L. Lovstakken, "Eigen-based clutter filter design for ultrasound color flow imaging: a review," *IEEE transactions on ultrasonics, ferroelectrics, and frequency control*, vol. 57, pp. 1096–1111, 2010.
- [14] C. Demene, T. Deffieux, M. Pernot, B. F. Osmanski, V. Biran, S. Franqui, and M. Tanter, "Spatiotemporal clutter filtering of ultrafast ultrasound data highly increases doppler and ultrasound sensitivity," *IEEE Transactions on Medical Imaging*, vol. 34, pp. 2271–2285, 2015.
- [15] P. Song, A. Manduca, J. D. Trzasko, and S. Chen, "Ultrasound small vessel imaging with block-wise adaptive local clutter filtering," *IEEE Transactions on Medical Imaging*, vol. 36, pp. 251–262, 2017.
- [16] M. W. Kim, Y. Zhu, J. Hedhli, L. W. Dobrucki, and M. F. Insana, "Multi-dimensional clutter filter optimization for ultrasonic perfusion imaging," *IEEE transactions on ultrasonics, ferroelectrics, and frequency control*, 2018.
- [17] M. Bayat, M. Fatemi, and A. Alizad, "Background removal and vessel filtering of noncontrast ultrasound images of microvasculature," *IEEE Transactions on Biomedical Engineering*, vol. 66, no. 3, pp. 831–842, 2019.
- [18] J. Tierney, C. Coolbaugh, T. Towse, and B. Byram, "Adaptive clutter demodulation for non-contrast ultrasound perfusion imaging," *IEEE Transactions on Medical Imaging*, vol. 36, pp. 1979–1991, 2017.
- [19] J. Tierney, K. Walsh, H. Griffith, J. Baker, D. Brown, and B. Byram, "Combining slow flow techniques with adaptive demodulation for improved perfusion ultrasound imaging without contrast," *IEEE transactions on ultrasonics, ferroelectrics, and frequency control*, vol. 66, pp. 834–848, 2019.
- [20] C. M. Gallippi, K. R. Nightingale, and G. E. Trahey, "Bss-based filtering of physiological and arfi-induced tissue and blood motion," *Ultrasound in medicine & biology*, vol. 29, no. 11, pp. 1583–1592, 2003.
- [21] J. E. Tierney, D. M. Wilkes, and B. C. Byram, "Independent component analysis-based tissue clutter filtering for plane wave perfusion ultrasound imaging," in *Medical Imaging 2019: Ultrasonic Imaging and Tomography*, vol. 10955. International Society for Optics and Photonics, 2019, p. 1095503.
- [22] J. Tierney, J. Baker, K. Ozgun, A. Borgmann, D. Brown, and B. Byram, "Non-contrast perfusion ultrasound imaging for assessment of trans-arterial chemoembolization for hepatic malignancy," in *2018 IEEE International Ultrasonics Symposium (IUS)*. IEEE, 2018, pp. 1–3.
- [23] A. Bell and T. Sejnowski, "An information-maximization approach to blind separation and blind deconvolution," *Neural Computation*, vol. 7, pp. 1129–1159, 1995.
- [24] H. Nielsen, "Ucminf - an algorithm for unconstrained, nonlinear optimization," IMM, Technical University of Denmark, Tech. Rep.

- IMM-TEC-0019, 2001. [Online]. Available: [http://www.imm.dtu.dk/pubdb/views/edoc\\_download.php/642/ps/imm642.ps](http://www.imm.dtu.dk/pubdb/views/edoc_download.php/642/ps/imm642.ps)
- [25] L. K. Hansen, J. Larsen, and T. Kolenda, "Blind detection of independent dynamic components," *In proc. IEEE ICASSP'2001*, vol. 5, pp. 3197–3200, 2001. [Online]. Available: [http://www.imm.dtu.dk/pubdb/views/edoc\\_download.php/827/pdf/imm827.pdf](http://www.imm.dtu.dk/pubdb/views/edoc_download.php/827/pdf/imm827.pdf)
- [26] S. Theodoridis and K. Koutroumbas, "Pattern recognition, edition," 2009.
- [27] E. L. Melnick and A. Tenenbein, "Misspecifications of the normal distribution," *The American Statistician*, vol. 36, no. 4, pp. 372–373, 1982.
- [28] Y.-m. Cheung and L. Xu, "Independent component ordering in ica time series analysis," *Neurocomputing*, vol. 41, no. 1-4, pp. 145–152, 2001.
- [29] A. Hendrikse, R. Veldhuis, and L. Spreuwers, "Component ordering in independent component analysis based on data power," in *Proceedings of the 28th Symposium on Information Theory in the Benelux, Enschede, The Netherlands*. Eindhoven, 2007, pp. 211–218.
- [30] E. H. Wu, L. Philip, and W. K. Li, "An independent component ordering and selection procedure based on the mse criterion," in *International Conference on Independent Component Analysis and Signal Separation*. Springer, 2006, pp. 286–294.
- [31] J. A. Jensen, "Field: A program for simulating ultrasound systems," *Med. Biol. Eng. Comput.*, vol. 34, pp. 351–353, 1996.
- [32] T. Loupas, J. T. Powers, and R. W. Gill, "An axial velocity estimator for ultrasound blood flow imaging, based on a full evaluation of the doppler equation by means of a two-dimensional autocorrelation approach," *IEEE Transactions on Ultrasonics, Ferroelectrics, and Frequency Control*, vol. 42, pp. 672–688, 1995.
- [33] D. B. Brown, B. Nikolic, A. M. Covey, C. W. Nutting, W. E. Saad, R. Salem, C. T. Sofocleous, and D. Y. Sze, "Quality improvement guidelines for transhepatic arterial chemoembolization, embolization, and chemotherapeutic infusion for hepatic malignancy," *Journal of Vascular and Interventional Radiology*, vol. 23, pp. 287–294, 2012.
- [34] G. Montaldo, M. Tanter, J. Bercoff, N. Benech, and M. Fink, "Coherent plane-wave compounding for very high frame rate ultrasonography and transient elastography," *IEEE Transactions on Ultrasonics, Ferroelectrics, and Frequency Control*, vol. 56, pp. 489–506, 2009.
- [35] Molares, "The generalized contrast-to-noise ratio," in *Proceedings of the IEEE International Ultrasonics Symposium*, Kobe, Japan, October 2018.
- [36] J. Baranger, B. Arnal, F. Perren, O. Baud, M. Tanter, and C. Demene, "Adaptive spatiotemporal svd clutter filtering for ultrafast doppler imaging using similarity of spatial singular vectors," *IEEE Transactions on Medical Imaging*, 2018.